Facile preparation of SrZr1-xTixO3 and SrTi1-xZrxO3 fine particles assisted by dehydration of Zr4+ and Ti4+ gels under hydrothermal conditions

J. R. Quiñones-Gurrola , J. C. Rendón-Angeles * , Z. Matamoros-Veloza , J. López-Cuevas , R. Pérez-Garibay , K. Yanagisawa

Posted Date: 6 July 2023

doi: 10.20944/preprints202307.0412.v1

Keywords: hydrothermal synthesis, gel dehydration, SrZrO3–SrTiO3, solid solution, crystallisation, cubic structure, orthorhombic structure

Article

Facile Preparation of $SrZr_{1-x}Ti_xO_3$ and $SrTi_{1-x}Zr_xO_3$ Fine Particles Assisted by Dehydration of Zr^{4+} and Ti^{4+} Gels under Hydrothermal Conditions

J. R. Quiñones-Gurrola [1], J. C. Rendón-Angeles [1,*], Z. Matamoros-Veloza [2], J. López-Cuevas [1], R. Pérez-Garibay [1] and K. Yanagisawa [3]

[1] Centre for Research and Advanced Studies of the National Polytechnic Institute, Saltillo Campus, Ramos Arizpe, 25900, Coahuila, México; jose.quinones@cinvestav.edu.mx; jcarlos.rendon@cinvestav.edu.mx; jorge.lopez@cinvestav.edu.mx; roberto.perez@cinvestav.edu.mx.

[2] Tecnológico Nacional de México/(I.T. Saltillo), Technological Institute of Saltillo, Graduate Division, Saltillo 25280, México; zully.mv2@saltillo.tnm.mx.

[3] Research Laboratory of Hydrothermal Chemistry, Faculty of Science, Kochi University, Kochi 780-8073, Japan; yanagi@kochi-u.ac.jp.

* Correspondence: jcarlos.rendon@cinvestav.edu.mx (J.C.R.A.); Tel.: +52 (844) 438 9600.

Abstract: In recent decades, perovskite-type compounds ($ABB'O_3$) have been exhaustively studied due to their unique ferroelectric properties. In this work, a systematic study aiming to prepare fine particles in the binary system $SrZrO_3$–$SrTiO_3$ was conducted under hydrothermal conditions in a KOH (5 M) solution at 200 °C for 4 h under a constant stirring speed of 130 rpm. The precursors employed were $SrSO_4$ powder (< 38 μm size) and coprecipitated hydrous gels of $Zr(OH)_4 \bullet 9.64\ H_2O$ (Zr-gel) and $Ti(OH)_4 \bullet 4.5H_2O$ (Ti-gel), which were mixed according to the stoichiometry of the $SrZr_{1-x}Ti_xO_3$ in the compositional range of 0.0>x>100.0 mol% Ti^{4+}. The XRD results revealed the formation of two crystalline phases rich in Zr^{4+}, an orthorhombic structured $SrZr_{0.93}Ti_{0.07}O_3$ and a cubic structured $SrZr_{0.75}Ti_{0.25}O_3$ within the compositional range of 0.1–0.5 mol of Ti^{4+}. A cubic perovskite-structured solid solution, $SrTi_{1-x}Zr_xO_3$, was preferentially formed within the compositional range of 0.5>x>0.1 mol% Ti^{4+}. The $SrZrO_3$ and $SrZr_{0.93}Ti_{0.07}O_3$-rich phases had particle sizes averaging 3 μm with a cubic morphology. However, a remarkable reduction in the particle size occurred on solid solutions prepared with hydrous Ti-gel over contents of 15 mol% Ti^{4+} in the reaction media, resulting in the formation of nanosized particles agglomerates with cuboidal shape self-assembled via a 3D hierarchical architecture, the sizes of these particles varied in the range between 141.0–175.5 nm. The limited coarsening of the particles is discussed based on the Zr-gel and Ti-gel dehydration capability differences that occurred under hydrothermal processing.

Keywords: hydrothermal synthesis; gel dehydration; $SrZrO_3$–$SrTiO_3$; solid solution; crystallisation; cubic structure; orthorhombic structure

1. Introduction

Perovskite structured oxide compounds with ABX_3 chemical formula have been investigated because of their broad practical applications and academic research interest. These are associated with their unique properties due to their relatively simple crystalline structure [1–3]. The cubic structural perovskite framework (*Pm3m*) comprises two linked coordination polyhedral networks, the BX_6 octahedra and AX_{12} cuboctahedra. Bonding between the BX_6 octahedra polyhedron and sites incorporating A cations occurs via corner-sharing. Interestingly, the BX_6 octahedra exhibit volumetric variations, namely expansion, contraction, and tilt, to maintain nonideal ionic size substitutions. Likewise, the local electronic instabilities can distort the octahedra or cause a slight cation shift from their unit cell structural positions. Perovskite structured materials allow ionic partial substitutions and the formation of vacancies on their three structural atomic locations [3]. Therefore, this structure is remarkably flexible to locate various periodic table elements at both A and B sites, resulting in a wide range of properties. The most important are ferroelectricity, ferromagnetism and colossal magnetoresistance, piezoelectricity and multiferroicity [3,4]. B-site cation doping has been one of the

Preprints (www.preprints.org) | NOT PEER-REVIEWED | Posted: 6 July 2023 doi:10.20944/preprints202307.0412.v1

major research subjects in developing new advanced perovskite materials; this site controls and tunes some of the most technologically attractive properties, such as electrical conductivity and magnetic order [5–8]. The tuning of these properties results from combining at least two elements, which maintain the cation structural ordering allowing to development of advanced new materials [3].

The perovskite binary system $SrTiO_3$–$SrZrO_3$, which has technological importance due to its dielectric properties [9], has attracted significant research interest for solid solution preparation via the B-site cation isomorphous substitution. The end members of this system, cubic $SrTiO_3$ (space group *Pm3m*) and orthorhombic $SrZrO_3$ (*Pbnm*), do not possess ferroelectric properties. However, the partial substitution of Zr^{4+} up to 5 mol% provided a remarkable increase in the dielectric breakdown strength (14.4 kV/mm), simultaneously maintaining the high dielectric constant (330) characteristic of $SrTiO_3$, which makes these materials suitable for technical applications as high voltage capacitors [9,10]. Likewise, the $SrTi_{1-x}Zr_xO_3$ microstructure mobility causes octahedral structural transitions, which consequently cause electronic changes resulting in a peculiar ferroelastic switching behaviour; this feature is essential for magnetic applications [13]. Similarly, the superlattice crystalline structures formed in $SrTi_{1-x}Zr_xO_3$ layered compounds achieve special BX_6 ordering that induces a two-dimensional tension mechanism, causing, at low temperatures, a ferroelectric Ti-rich solid solution (SS) Ti [13]. To some extent, the structural distortion somewhat might promote the proton motion [14]. Another potential technical application determined for ultrafine powders of $SrTi_{1-x}Zr_xO_3$ solid solutions SS include photoluminescence emission [15] and organic dye photocatalysts [16].

Various systematic studies have been focused on the SS-$SrTi_{1-x}Zr_xO_3$ preparation in the $0.0 \geq x \leq 0.5$ mol% Zr^{4+} compositional range by the conventional high-temperature solid-state reaction [1,4,6,8,10,11]. The powders were produced by mixing high-purity $SrCO_3$, TiO_2 and ZrO_2 powders, which were appropriately mixed in stoichiometric molar ratios to form a slurry with acetone. The powder mixtures were homogenised by vigorous grinding and then pressed. The pellets underwent calcination in a three-step heat treatment between 800 and 1400 °C for 24 to 96 h reaction intervals. However, the SS-$SrTi_{1-x}Zr_xO_3$ monodisperse nanoparticle formation was not feasible under the conventional ceramic processing route.

On the contrary, chemical solution processing techniques, namely sol-spray pyrolysis [5], low-temperature coprecipitation [7], and sol-gel [16], successfully achieved the preparation of $SrTi_{1-x}Zr_xO_3$ nanoparticles with accurate stoichiometric compositions, controlled morphology and monomodal particle size distributions that boosted their physical and chemical properties [5,7,16]. Furthermore, the hydrothermal technique has successfully prepared $SrTiO_3$ mesocrystals with nanoparticle sizes and controlled cubic morphology [17–19]. The systematic studies focused on the chemical reaction of a slurry media containing TiO_2 particles and $Sr(OH)_2$ hydrolysed in a highly alkaline NaOH media (5–10 M) under hydrothermal conditions, resulting in the formation of the $SrTiO_3$ nanoparticles via two mechanisms, namely the topochemical transformation of the TiO_2 particles [17,18] and the conventional dissolution-precipitation process [19]. A different approach involving the employment of a mineral source as Sr^{2+} ($SrSO_4$) precursor and hydrous Ti-gel ($Ti(OH)_4 \bullet 4.5H_2O$) was also evaluated under hydrothermal conditions at 250 °C for 24 h in a KOH solution 5 M [20]. Under these conditions, the dissolution of the $SrSO_4$, coupled with the Ti-gel dehydration, established the chemical equilibrium for triggering the crystallisation of monodispersed fine cubic-shaped $SrTiO_3$ crystals, which exhibited a monomodal particle size distribution. This process can reduce global production costs compared to the low-temperature chemical solution processing and the conventional hydrothermal technique, which uses pure Sr^{2+} chemical reagents produced from the celestite mineral.

A literature review suggests that further efforts must be made to investigate the feasibility of producing $SrZr_{1-x}Ti_xO_3$ or $SrTi_{1-x}Zr_xO_3$ solid solution via hydrothermal alkaline processing. Hence, this work systematically investigated the preparation of particles with different chemical compositions in the binary $SrZrO_3$-$SrTiO_3$ system in alkaline media (5 M KOH). The experiments were conducted at a standard temperature (200 °C), which is relatively low for rapidly dissolving the $SrSO_4$ particles, and seemingly vertical agitation might provide an adequate dispersion of the mineral particles and precursor gels in the alkaline solvent solution during the treatment. Particular emphasis was on determining the effect of the precursor gels (Zr-gel and Ti-gel) dehydration capability on the

 doi:10.20944/preprints202307.0412.v1

particle crystallisation of both $SrZr_{1-x}Ti_xO_3$ and $SrTi_{1-x}Zr_xO_3$ (SS). A detailed analysis was made to determine the stability of the tetragonal structure in the compositional $2.5 \geq x \leq 50.0$ mol% of Ti^{4+} for the $SrZr_{1-x}Ti_xO_3$ samples. The nanoparticle size and morphological differences were correlated with the dehydration capability of the gels.

2. Materials and Methods

2.1. Materials and preparation of Zr^{4+} and Ti^{4+} precursor gels

Reagent-grade zirconium IV ($ZrCl_4$) and titanium IV ($TiCl_4$) chlorides (Wako, Japan, 99.0% purity) were used for preparing the precursor gels. Initially, the transition metal precursor solutions were produced with a concentration of 0.43 M for $ZrCl_4$ and $TiCl_4$ with deionised water, following the procedure described elsewhere [20], respectively. A 500 ml liquor aliquot of each solution was poured into a glass beaker, and then the gels were precipitated by adding a volume of 150 ml of 5 M NaOH solution. Each gel was separated from the residual mother liquor by centrifugation. The thermogravimetry analysis determined the total weight loss of each gel, indicating that the chemical composition of the hydrous gels corresponds to $Zr(OH)_4 \bullet 9.64H_2O$ and $Ti(OH)_4 \bullet 4.5H_2O$, respectively. The $SrSO_4$ mineral (Celestite) crystals were previously grounded and pulverised to a particle size < 38 μm. The wet chemical analysis of the highly pure crystalline $SrSO_4$ (1 g) revealed that the mineral is constituted by 46.61 wt% Sr, 1.33 wt% Ba, and 52.05 wt% SO_4^{2-}, which correspond to 96.8 wt% $SrSO_4$ and 2.25 wt% $BaSO_4$, plus the following minor compounds were CaO (0.73 wt%), Fe_2O_3 (0.19 wt%), MnO (0.02 wt%) and Al_2O_3 (0.007 wt%). The alkaline reagent-grade chemical employed was KOH (Wako, Japan, 99.0% purity)

2.2. Hydrothermal treatments

Experiments aimed to determine the feasibility of producing stable $SrZr_{1-x}Ti_xO_3$ and $SrTi_{1-x}Zr_xO_3$ and to elucidate the SS crystalline structural and microstructural features, which might vary due to transition metal gel dehydration process that occurs under alkaline stirring hydrothermal conditions. Therefore, the synthesis of the solid solutions in the binary $SrZrO_3$–$SrTiO_3$ system proceeded in the entire compositional range. However, a particular emphasis took place on the molar content of $1.0 \geq x \leq 0.5$ of Zr^{4+} to investigate the tetragonal structure stability; this crystalline structure is predominant at temperatures lower than 400 °C [5,10]; thus, the compositions studied varied in a molar span of 2.5 mol% Zr^{4+}. A $SrSO_4$ powder sample (4.8 ± 0.05 g) was placed at the bottom of a Teflon test tube type chamber (500 ml volume), the amount of each gel was calculated according to the chemical formulas mentioned in section 2.1, and the stoichiometric Zr:Ti molar ratio 1-x:x, was then added. All the treatments were conducted at a constant volume (95 ml) of the 5 M KOH solution selected as a solvent media. The stainless-steel autoclave was sealed, and the vertical propel rotation set was at 130 rpm during the heating and soaking stages (Figure 1). The autoclave was then heated at a constant speed of 5 °C/min up to the selected temperature of 200 °C. The treatments were conducted at this temperature for 4 h. After treatment, the reaction products were separated from the remaining mother liquor and ultrasonically washed several times with hot water. Then, the powders were dried at 80 °C overnight.

Preprints (www.preprints.org) | NOT PEER-REVIEWED | Posted: 6 July 2023 doi:10.20944/preprints202307.0412.v1

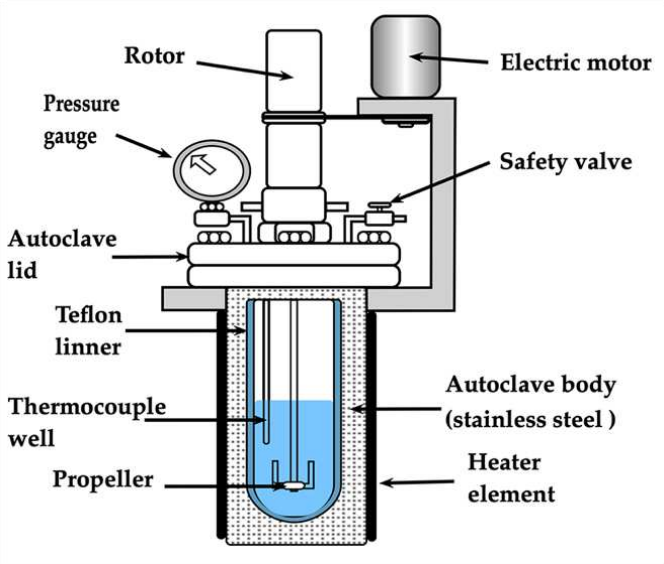

Figure 1. Scheme of the stainless-steel vessel accoupled with a vertical stirring propel and internal Teflon liner tube with a capacity of 500 ml.

2.2. Characterisation

Powder X-ray diffraction (PXRD). The analyses were conducted in a Rigaku Ultima IV diffractometer operated at 40 kV and 20 mA, using Cu-Kα radiation (λ = 1.54056 Å). XRD analyses were collected in the 2θ range of 5–80° at a constant scanning speed of 20 °/min with a 0.02° step. Rietveld refinement analyses were carried out on the PXRD patterns collected in the 2θ range of 15–130°, under standard conditions at a scanning speed of 0.01°/min and 0.002° step. The refinement calculations were performed using the TOPAS 4.2 software (Bruker AXS: Karlsruhe, Germany, 2009). The space group, and the atomic position (Wyckoff number and coordinates), correspond to the COD card No. 96-900-7150. Additional details associated with the Rietveld refinement analysis are in the supplementary supporting information file, Section S2.3.

Morphology and microstructural observation. The microstructural aspects of the produced particles were observed in a field emission scanning electron microscopy (JEOL JSM-7100F) equipped with a solid-state microprobe (EBSD, Bruker e-flash). Typical micrographs were observed with the microscope operated at 10 kV and a constant current of 69 μA. The particle size distribution was statistically determined from SEM images of 50 particles. Crystalline structural details of selected $SrZr_{1-x}Ti_xO_3$ particles were revealed using high-resolution transmission electron (HR-TEM, Philips Titan 300) operated at 200 kV.

Differential scanning calorimetry analysis (DSC). The DSC technique was applied to determine the thermal behaviour of single Zr-gel and Ti-gel and some selected samples with varied Zr/Ti weight ratios. These analyses also revealed the differences in the dehydration behaviour of the Zr/Ti raw gel mixtures. Simultaneously, the gel sample weight variation was determined by thermogravimetric analysis. These analyses were carried out using a Perkin Elmer Pyris Diamond TG/DSC apparatus in the temperature range from 30 to 1000 °C. The heating rate selected for the thermal evaluation was 10 °C/min; all the treatments were conducted using an air atmosphere.

3. Results

3.1. Thermal stability of gel mixtures and Zr-gel and Ti-gel

Thermogravimetry and DSC analyses were conducted to evaluate the thermal stability and structural changes of single pasty Zr-gel, Ti-gel and some selected gels mixtures containing different Zr/Ti ratios. These analyses aimed to determine the total weight loss monitored in the air atmosphere within the 30–1000 °C temperature range. The change in the weight of the gels is portrayed in Figure 2a. In general, the gels selected exhibited a remarkable weight loss above 50 °C, without further

Preprints (www.preprints.org) | NOT PEER-REVIEWED | Posted: 6 July 2023 doi:10.20944/preprints202307.0412.v1

weight variation above 150 °C. Interestingly, the Zr pure gel had the most significant weight loss of approximately 90.93 wt%; in comparison with that observed for the Ti pure (67.2 wt%) and Zr/Ti (75.5–80.0 wt%) gel samples. According to the total amount of water that Zr and Ti pure gels released during the heat treatment, their chemical formulas are $Zr(OH)_4 \bullet 9.64H_2O$ and $Ti(OH)_4 \bullet 4.5H_2O$, respectively.

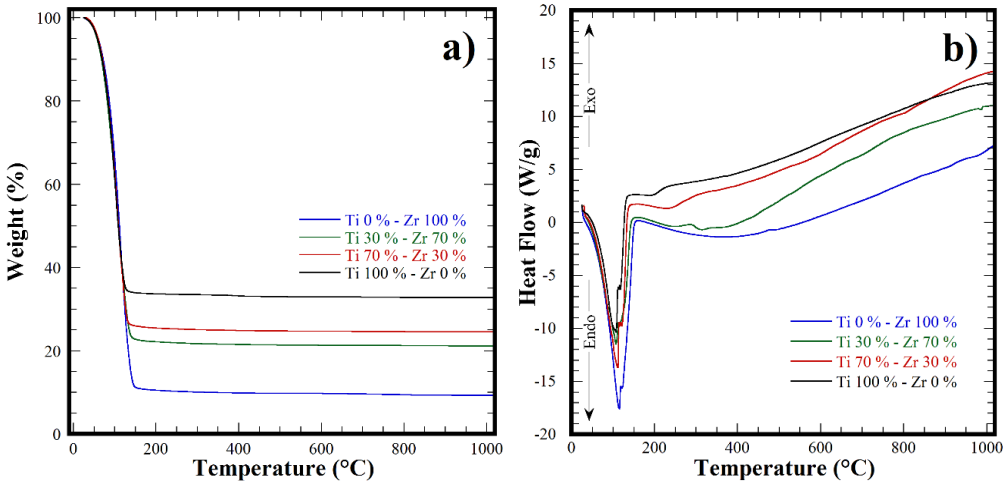

Figure 2. a) Weight lost variation and b) thermal behaviour of the precursor Zr-Ti gels determined by DSC in air atmosphere up to 1000 °C.

Furthermore, the thermal behaviour of all the Zr-Ti gels observed in the DSC curves (Figure 2b) revealed an endothermic event in the temperature range from 45–150 °C. This event is irrespective of the pasty gel chemical composition; therefore, this peak correlates with the water molecules' ultimate dehydration process. Above 200 °C, only a regular baseline variation was observed on all samples rather than the expected crystallisation events associated with the oxide formation on all the gels. Moreover, the differences in the dehydration degree determined might alter the bulk concentration of the alkaline fluid used during the hydrothermal treatments conducted under the standard hydrothermal conditions of 200 °C for 4 h under stirring. This agrees with the differences in the crystal growth of the $SrZrO_3$ particles hydrothermally synthesised using a pasty Zr-gel and a previously dried amorphous $Zr(OH)_4^0$ reported elsewhere [21].

3.2. Structural aspects of the hydrothermal synthesis of $SrZr_{1-x}Ti_xO_3$ and $SrTi_{1-x}Zr_xO_3$ SS

Figure 3 shows the typical XRD patterns of selected powders produced under hydrothermal conditions at 200 °C for 4 h under constant stirring (130 rpm), varying the content of Ti^{4+} in the mixture. Generally, the single-step chemical reaction between the $SrSO_4$ and the pasty gels is enhanced under stirring conditions, triggering the formation of a fine white powder, as confirmed in all treatments by naked-eye observations. When the Zr-gel was solely used as a precursor of the tetravalent metal perovskite, the peaks in the XRD pattern were indexed by those of the $SrZrO_3$ perovskite with orthorhombic structure (ICDD 70-0283 space group *Pbnm*, Figure 3a). On the contrary, at Ti^{4+} contents over 10.0 mol%, new peaks located at 2θ angles of 32.25°, 39.7°, 45.8° and 56.9° were determined in the PXRD pattern, as seen in Figure 3a. To determine the formation pathway of the new compound, experiments were conducted with a Ti^{4+} compositional span variation of 2.5 mol% Ti^{4+}. The new phase was formed under alkaline hydrothermal conditions in the Ti^{4+} compositional range between 7.5 and 47.5 mol% Ti^{4+}, as depicted by the signal that appeared at 32.25° 2θ angle (see Figure 3b). It deserves emphasising that this peak exhibited a gradual shift toward higher 2θ angles coupled with peak intensity increment. These crystalline structural features are likely due to the Ti^{4+} gradual incorporation into the crystalline structure, and its bulk content produced over 7.5 mol% Ti^{4+} contents in the reaction media. Simultaneously, the central peak corresponding to the orthorhombic structured $SrZrO_3$:Ti^{4+} (SS1) did not exhibit further compositional

Preprints (www.preprints.org) | NOT PEER-REVIEWED | Posted: 6 July 2023 doi:10.20944/preprints202307.0412.v1

variations because it remained at a mean 2θ angle of 31.09°. Therefore, these results suggest that the chemical composition of this solid solution is $SrZr_{0.925}Ti_{0.075}O_3$. However, the content of this stable phase was proportionally reduced by increasing the Ti^{4+} amount, as indicated by the progressive reduction of the orthorhombic phase peaks in the PXRD pattern (Figure 3a). Above 50.0 mol% Ti^{4+} peaks corresponding to a new secondary SS2 phase were obtained. Based on these structural results, we infer that the crystalline structure of the SS2 single-phase can be indexed with the cubic structured $SrTiO_3$ perovskite (space group *Pm3m*, ICDD card no. 40-1500) because it agrees with the peaks distribution of the $SrTiO_3$ single pattern. These results depict that the cubic perovskite SS2 crystalline phase is chemically stable under hydrothermal conditions in the compositional range of 7.5–100.0 mol% Ti^{4+}. In addition, the powder crystallised without contaminant by-products, namely $SrCO_3$, which is predominantly formed due to its low solubility in alkaline solutions [22]. Furthermore, a steady-state chemical reaction involving the solute saturation of the hydrothermal media is likely to proceed and trigger the simultaneous crystallisation of both crystalline compounds under fluid stirring [23].

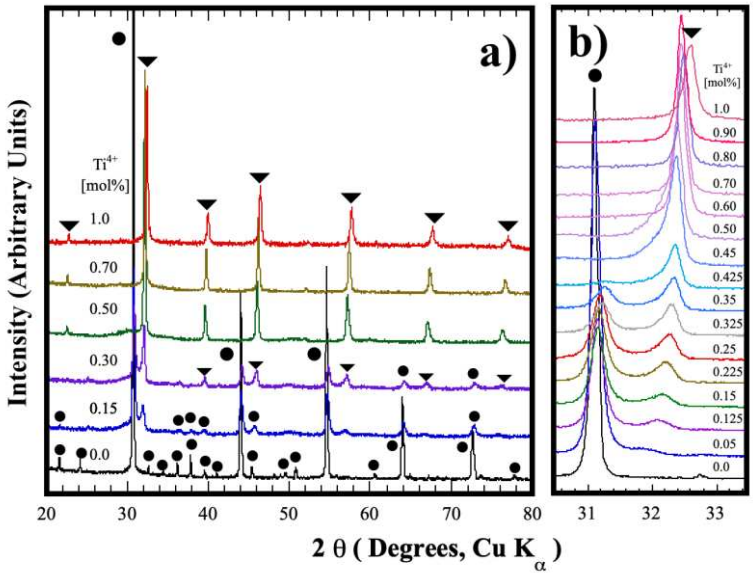

Figure 3. (a,b) X-ray diffraction patterns of the products obtained hydrothermally by treating celestite powders with various molar contents of pasty $Zr(OH)_4 \bullet 9.64H_2O$ and $Ti(OH)_4 \bullet 4.5H_2O$ gels, with a solvent (5 M KOH) volume filling ratio of 20 % at 200 °C for 4 h. Perovskite single phases: (●) Orthorhombic $SrZrO_3$, and (▼) Cubic $SrTiO_3$.

The compositional variation suggested by the PXRD analyses was observed in the SS2 phase. Stoichiometric computation was carried out to determine the Ti^{4+} content incorporated in the cubic perovskite secondary SS2 phase and into the orthorhombic SS1; this procedure considered the nominal Ti^{4+} molar content added as a raw material. Likewise, the fraction of each solid solution that constitutes the ultimate powder produced was calculated by the expression [(1-x)SS1 + xSS2'] = 1, which depicts the quantitative variation in the phase content revealed by the diffraction patterns of Figure 3b. The typical Rietveld refined plots that correlate the quantitative stoichiometric computation abovementioned are shown in Figure 4. Interestingly, a minimal variation of the residual difference was also revealed in those samples exhibiting the formation of SS1 and SS2 perovskite phases. These results show that the calculated Zr^{4+}:Ti^{4+} stoichiometric contents in the orthorhombic and cubic phases with *Pbnm* and *Pm3m* space groups highly fitted the atomic occupation in the Rietveld refinement algorithm. The algorithm ultimately computed the fraction content of each perovskite phase in the powder sample prepared with nominal molar Zr^{4+}:Ti^{4+} ratios of (a) 92.5:7.5 (b) 75.0:25.0 and (c) 62.5:37.5, as it can be seen in Figure 4. Furthermore, the structural crystalline refinement approach also considered other fitting parameters such as background, thermal isotropy, lattice parameters, scale factor, profile half-width, crystallite size and local strain;

Preprints (www.preprints.org) | NOT PEER-REVIEWED | Posted: 6 July 2023 doi:10.20944/preprints202307.0412.v1

the details regarding the atomic Wyckoff elemental spatial distribution are given in the supplementary supporting information file, which includes Table S1 that summarises the results of the crystalline structural refinement. This approach was adequate to fit the structural differences of the reaction products obtained after the hydrothermal reaction, which is depicted by both the low mean values of the goodness-of-fit factor (GOF, mean χ^2 value of 3.48%) and R_{wp} = 3.26. It deserves to emphasise that the analyses confirmed that the orthorhombic and cubic crystalline perovskite particles were simultaneously formed under hydrothermal conditions employing the highly soluble $SrSO_4$ powder and the mixture of Zr^{4+} and Ti^{4+} gels.

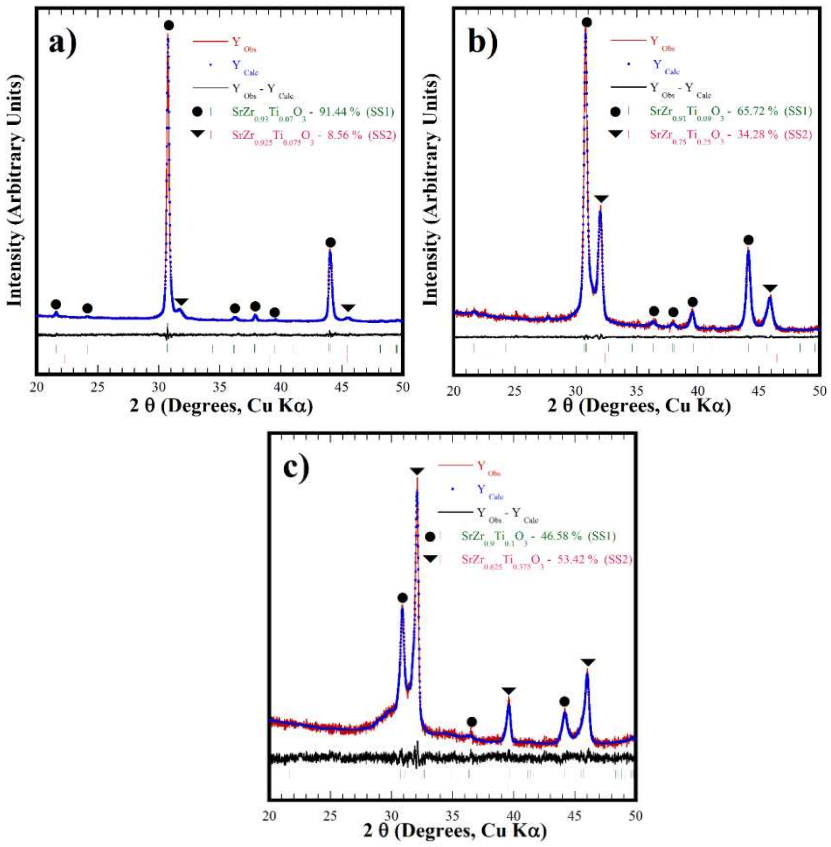

Figure 4. Rietveld refinement plots of products obtained hydrothermally using celestite powders mixed with different metal precursor gels in molar ratios of (a) 92.5:7.5, (b) 75.0:25.0 and (c) 62.5:37.5 mol% Zr^{4+}:Ti^{4+}, with a solvent (5 M KOH) volume filling ratio of 20 % at 200 °C for 4 h. Perovskite single phases (●) Orthorhombic and (▼) Cubic.

The variation in the content of both orthorhombic and cubic structured solid solutions, which were hydrothermally produced within the whole compositional range of the binary system $SrZrO_3$-$SrTiO_3$; using a KOH 5 M solution, is portrayed in Figure 5a. Generally, the formation of the new cubic perovskite phase (SS2′) occurred in the compositional range between 7.5 mol% and 47.5 mol% Ti^{4+}. The quantitative analyses conducted on the nominal stoichiometric tetravalent metal compositions depict that the new cubic SS2′ phase reach in Zr^{4+} ($SrZr_{1-x}Ti_xO_3$) exhibited a marked increase in its content when the Ti^{4+} concentration increased progressively in the solvent fluid. Interestingly, the variation in the bulk content of this phase likely resembles a typical sigmoidal kinetic behaviour. On the contrary, the residual content of the hydrothermally crystallised orthorhombic phase (SS1) powder proportionally decreased following a reverse sigmoidal behaviour. The simultaneous crystallisation of both perovskite phases is likely triggered under hydrothermal conditions because the continuous gel dehydration promotes a cooperative reaction steady state; thereby, a constant increase in the Ti^{4+} mass gradient provoked a rise in the cubic SS2′ single phase amount. This inference is supported by the fact that the Zr^{4+} atomic ratio in the SS2′ cubic phase exhibited a linear decrease, proportional to the rise of the Ti^{4+} content, as seen in Figure 5b.

Preprints (www.preprints.org) | NOT PEER-REVIEWED | Posted: 6 July 2023 doi:10.20944/preprints202307.0412.v1

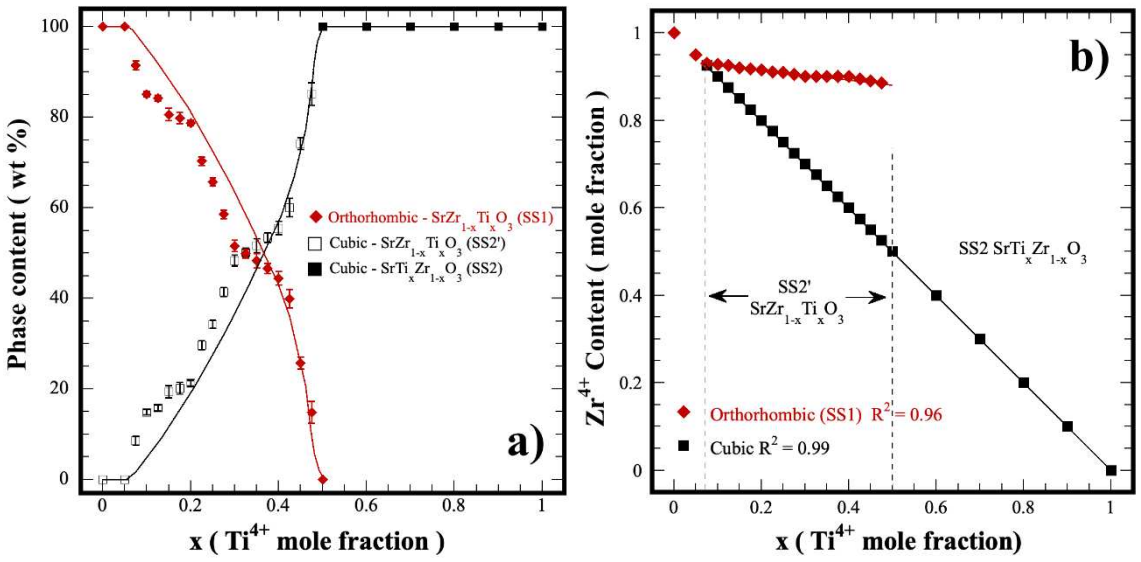

Figure 5. (a) Kinetic curves related to the variation of the solid solution contents, and (b) change in the Zr^{4+} molar fraction in both the orthorhombic and cubic perovskite solid solutions within the whole compositional range of the binary system $SrZrO_3$-$SrTiO_3$.

Furthermore, the orthorhombic SS1 phase showed a slight reduction of 4.0 mol % in the amount of Zr^{4+} within the compositional range where both crystalline phases coexist in the binary system $SrZrO_3$-$SrTiO_3$. According to these compositional results, three chemical reaction equilibria drive the crystallisation of chemically stable perovskite SS in the hydrothermal system studied. These are included in the supplementary supporting information file.

Additionally, details on the crystalline unit cell, lattice parameters and volume cell, corresponding to the perovskite solid solutions, which were produced under hydrothermal conditions in a 5 M KOH solution at 200 °C for 4 h with a constant stirring speed of 130 rpm, are portrayed in the graphs in Figure 6. Generally, the lattice constants corresponding to the end members of the perovskite binary system $SrZrO_3$-$SrTiO_3$ are slightly higher in comparison with the values reported in Table S3 (SSFI) for the same compounds. Meanwhile, a marked continuous decrease of "a_0", "b_0", and "c_0" parameters was determined in the orthorhombic solid solution (SS1, ●), with *Pbnm* space group, by increasing the Ti^{4+} content uptake in the resulting crystalline particles, as seen in Figure 6a. Likewise, the "a_0" lattice parameter corresponding to the new cubic SS2′ and SS2 (■) constituents (space group *Pm3m*) exhibited a linear decrease within the Ti^{4+} compositional variation, which occurred within the ranges of $7.5 \geq x \leq 50.0$ mol% Ti^{4+} and $50.0 \geq x \leq 100.0$ mol% Ti^{4+}, as seen in Figure 6a. In both cases, the variation determined for lattice parameter values of either orthorhombic or cubic perovskite structures agree with the systematic peak displacement determined in the X-ray results shown in Figure 3. Interestingly, all the lattice constants calculated exhibited a linear variation, which is depicted by the mean data dispersion coefficient R^2 that varied between 0.912 and 0.987. This behaviour indicates a linear dependence of the structural parameters occurred by incorporating Ti^{4+} content in the orthorhombic and cubic structured perovskite compound produced under hydrothermal conditions. Furthermore, the linear variation of the lattice parameters agrees with Vegard's law, despite two simultaneous perovskite-related compounds crystallising within the compositional range of $7.5 \geq x \leq 50.0$ Ti^{4+} mol%. Therefore, in the context of the chemical composition, the processing approach investigated is devoted to determining the chemical reaction pathway related to the formation of stable perovskite solid solution compounds in the binary system $SrZrO_3$-$SrTiO_3$; the results suggest that a steady-state single-step reaction is triggered under stirring hydrothermal condition, preferentially crystallise two solid solutions at the B site of the perovskite $SrZr_{1-x}TiO_3$ with orthorhombic and cubic structures. The reaction pathway is likely controlled by the tetravalent metal gel dehydration process inherent to the proposed system.

Preprints (www.preprints.org) | NOT PEER-REVIEWED | Posted: 6 July 2023 doi:10.20944/preprints202307.0412.v1

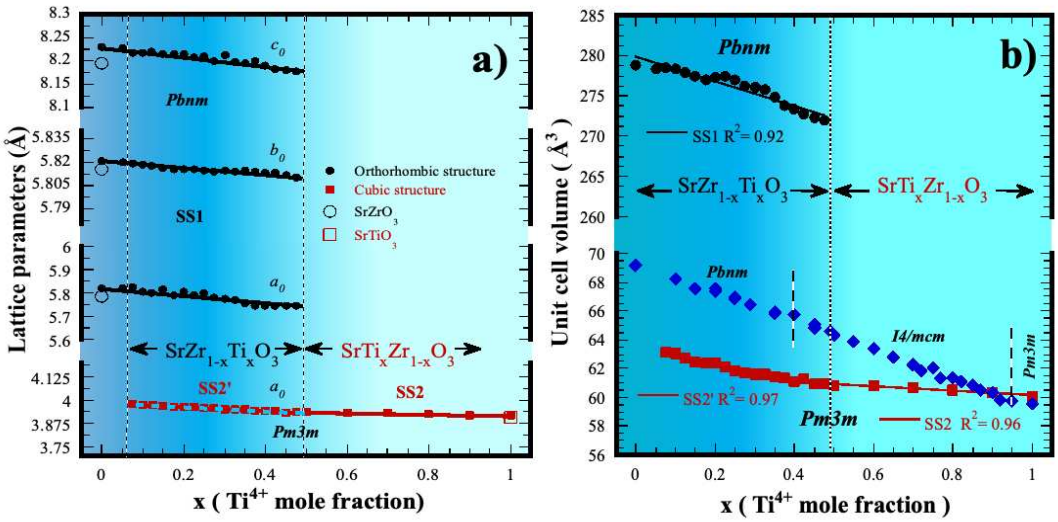

Figure 6. Variation of the crystalline structural parameters for the orthorhombic (SS1) and cubic (SS2′ and SS2) perovskite structured solid solutions prepared under hydrothermal conditions at 200 °C for 4 h with stirring at 130 rpm. (a) Unit cell lattice parameters and (b) unit cell volume. ◆ Unit cell values of $SrZr_{1-x}Ti_xO_3$ and $SrTi_{1-x}Zr_xO_3$ solid solutions produced at a high temperature within the entire compositional range of the binary system $SrZrO_3$–$SrTiO_3$; data taken from [8].

In addition, a similar trend was observed for the lattice constants variation for the unit cell volume of the perovskite solid solutions. These values are portrayed in the plot shown in Figure 6b, and this plot also includes the unit cell volume values calculated for the $SrTi_xZr_{1-x}O_3$ (solid ◆ symbol) solid solutions prepared at 1400 °C for 96 h [8]; these data were included for comparison purposes. Some data are likely similar to those determined in our case, namely at Ti^{4+} contents above ≤ 90.0 mol%. The authors demonstrate that the formation of stable solid solution preferentially occurs within the entire compositional range of the system $SrZrO_3$-$SrTiO_3$, as depicted by the data plotted in Figure 6b. Exhaustive crystalline structural analyses conducted by neutron and synchrotron diffraction confirmed the dependence of the SS´s composition with the crystalline structural transformations, which leads to obtaining orthorhombic, tetragonal and cubic structures stable at specific Ti^{4+} contents incorporated into the SS $SrTi_xZr_{1-x}O_3$. Superlattice reflections revealed near 2θ = 33 and 41° (021 and 122/212 Miller indexes) corresponding to the orthorhombic structure were detected up to 40.0 mol% Ti^{4+}; above this content, tetragonal structure predominates as sole phase produced at high temperature, the new reflection at 2θ ≈ 40° (121) confirmed the formation of $SrTi_xZr_{1-x}O_3$ SS that belongs to this structure, which predominates at the highest Ti^{4+} content of 90.0 mol% at low temperature [8].

Interestingly, the PXRD analyses conducted on the hydrothermally prepared specimens with Ti^{4+} contents between 7.5 mol% and 90.0 mol% did not reveal the superlattice peaks associated with the perovskite tetragonal structure, despite the observation of a similar variation trend on the unit cell volume of both reaction products with orthorhombic and cubic structures prepared here, compared with the continuous solid solutions obtained via solid-state reaction at high temperature [8]. We infer from these results that the Ti-gel dehydration yield plays an essential role in achieving a steady-state chemical reaction, which enhances a specific solute supersaturation stage that causes the simultaneous crystallisation of both phases. This process proceeds faster than the solid-state reaction producing a broad compositional series of solid solutions in the system $SrZrO_3$–$SrTiO_3$ [8].

On the other hand, according to the crystalline structural results calculated by Rietveld refinement given in the Table S3 of the SSI file, the minor structural differences revealed on the unit cell parameters in both perovskite compounds (orthorhombic and cubic) are caused by the variation in the Sr-O, Ti-O and Zr-O bond lengths. A systematic increase in the Ti-O bond length proportionally occurred by decreasing the Ti^{4+} content incorporated into the octahedral BO_6 site in the cubic

 doi:10.20944/preprints202307.0412.v1

structured SS2, in the compositional range of $7.5 \leq x \leq 90$ mol% Ti^{4+}. Similarly, the Sr-O bond length is considerably affected, reaching a maximum value of 2.822 Å, which is remarkably more extensive than that for the cubic structured $SrTiO_3$ single phase (2.769 (1) Å, as seen in Table S3). From these results, we surmise that this structural phenomenon maintains the cubic structured solid solution thermodynamically stable at low contents of Ti^{4+} below 50.0 mol%. This inference is supported by the fact that under solid-state reaction conditions, a series of intermediate tetragonal structured solid solutions were successfully formed in a shorter range of Ti^{4+} ($40.0 \leq x \leq 90.0$ mol% Ti^{4+}). It deserves to emphasise that the tetragonal structure remains stable because it corresponds to the primitive cell of the orthorhombic structured perovskite. Therefore, this structural transformation is favoured by a slight structural tilt in the BO_6 octahedra caused by the Ti^{4+} partial incorporation. This structural transformation is markedly provoked under solid-state reaction conditions at high temperatures [8]. Another factor that might cause the predominant formation of the SS2 solutions with cubic structure and their structural variations is associated with the processing conditions (reaction temperature and stirring speed), as suggested elsewhere [21]. This inference is likely supported by the marked differences determined for the lattice strain caused in the unit cell by the partial incorporation of Ti^{4+} in the cubic SS2′ SS. Large lattice strain values were calculated from the Rietveld refinements for the SS2′ SS prepared with Ti^{4+} contents between 7.5 and 50 mol% and are shown in Table S3 of the supplementary supporting information.

3.3. Particle morphology variation for the hydrothermally synthesised $SrZr_{1-x}Ti_xO_3$ and $SrTi_{1-x}Zr_xO_3$ (SS)

Recently, the morphological habit features for $SrZrO_3$ particles were elucidated; the hydrothermal treatments conducted without stirring in an alkaline media (5 M KOH) using the same reaction precursors resulted in the crystallisation of micron-sized (averaging 10 μm) $SrZrO_3$ particles with cuboidal morphology [21]. On the contrary, our results depicted that continuous stirring (130 rpm) of the hydrothermal media remarkably improved the size reduction of the cuboidal-like $SrZrO_3$ particles, which were produced free of reaction by-products, namely $SrCO_3$, at 200 °C for 4 h. The monodispersed $SrZrO_3$ particles had a unimodal particle size distribution with an average size of 3.8 μm, as seen in the inlet graph of Figure 7a. Under these conditions, the continuous agitation caused a homogeneous distribution of solute dissolved in the alkaline solvent.

Preprints (www.preprints.org) | NOT PEER-REVIEWED | Posted: 6 July 2023 doi:10.20944/preprints202307.0412.v1

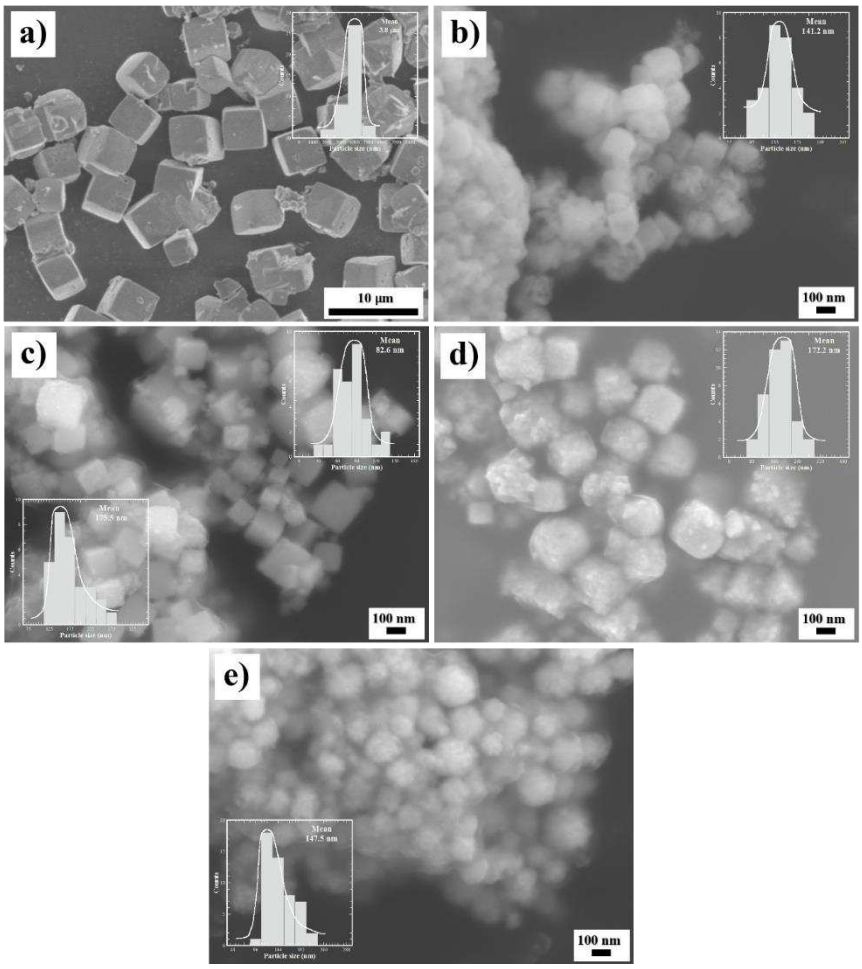

Figure 7. FE-SEM micrographs of the particles of the $SrZr_{1-x}Ti_xO_3$ and $SrTi_{1-x}Zr_xO_3$ solid solutions, obtained under dynamic hydrothermal conditions at 200 °C in a reaction medium of 5 M KOH for a reaction time of 4 h, using $SrSO_4$ and different ratios of Zr and Ti gels ($Zr(OH)_4 \bullet 9.64H_2O$, $Ti(OH)_4 \bullet 4.5H_2O$). a) $SrZrO_3$, (b) 5.0 mol% Ti^{4+}, (c) 30.0 mol% Ti^{4+}, (d) 50.0 mol% Ti and (e) $SrTiO_3$.

On the contrary, a marked particle reduction occurred on the perovskite particles produced when the Ti^{4+} pasty gel was stoichiometrically introduced into the reaction system. Above Ti^{4+} contents of 5.0 mol%, the single phase $SrZr_{0.95}Ti_{0.05}O_3$ powders exhibited a mean particle size of 141.2 nm. The morphology resembling cuboidal-shaped particles forming some irregularly shaped agglomerates, Figure 7b. Furthermore, the formation of a noticeable number of fine meso-crystals (average size 82.6 nm) with a pseudo cuboidal shape were formed together with a large amount of cubic-like shaped large particles having an average size of 175.5 nm, Figure 7c. It deserves to emphasise that these particles were formed using the content of 30 mol% Ti^{4+}, and the FE-SEM observation agrees with the PXRD results which revealed the coexistence of two $SrZr_{1-x}Ti_xO_3$ solutions with different Ti^{4+} content (Figure 3a). Likewise, the difference on the $Zr_{(L\alpha)}$ and $Ti_{(K\alpha)}$ peak intensities between the fine sized pseudo cuboidal and large cubic-like particles confirmed the variation on the bulk chemical composition of the SS1 and SS2′ (as seen in Figure S3b in SSI file). Based on the Rietveld refinement analyses, their chemical formulas correspond to $SrZr_{0.9}Ti_{0.1}O_3$ and $SrZr_{0.70}Ti_{0.3}O_3$, respectively.

The pseudocubic meso-crystals were formed preferentially under hydrothermal stirring conditions with Ti^{4+} contents over 50 mol%. Generally, the new pseudocubic-shaped meso-crystals were monodispersed and exhibited a unimodal size distribution with an average size of 172.2 nm. Furthermore, the single-phase $SrZr_{0.5}Ti_{0.5}O_3$ (SS2) cubic structured meso-crystals were likely formed from tiny particles self-assembled via a 3D hierarchical architecture; this assumption was inferred from the roughness surface of the meso-crystals shown in Figure 7d. Additionally, the FE-SEM

Preprints (www.preprints.org) | NOT PEER-REVIEWED | Posted: 6 July 2023 doi:10.20944/preprints202307.0412.v1

observations conducted on the hydrothermally produced single phase $SrTiO_3$ meso-crystals (see Figure 7e), allowed to infer that these meso-crystals underwent a crystallisation process analogous to that observed on samples containing low contents of Ti^{4+} up to 50.0 mol%. Thus, the meso-crystals solely prepared with $Ti(OH)_4^0$ gel had a slight reduction in their particle size, which averaged 147.5 nm. According to the experimental results, it can be inferred that the chemical compositional variation in the crystalline phases produced (SS1, SS2' and SS2) and the particle coarsening differences are strongly dependent on the $Ti(OH)_4^0$ gel content variation in the hydrothermal treatments conducted under vigorous agitation. Details of the crystallisation mechanism and its correlation with the precursor gels ($Zr(OH)_4^0$ and $Ti(OH)_4^0$) are discussed in the following section 3.4.

3.4. Crystallisation of $SrZr_{1-x}Ti_xO_3$ and $SrTi_{1-x}Zr_xO_3$ meso-crystals under alkaline hydrothermal conditions

HR-TEM observations and compositional EDS analyses systematically investigated the crystallisation process for both $SrZr_{1-x}Ti_xO_3$ and $SrTi_{1-x}Zr_xO_3$ promoted under hydrothermal treatment conducted with vigorous fluid agitation, according to the differences in morphology revealed by the FE-SEM analyses (Figure 7, and Figure S4 in the SSI), the growth process of the meso-crystals depends on the $Ti(OH)_4^0$ gel. This inference is supported by the remarkable reduction of either Zr^{4+} rich orthorhombic or cubic structured particles preferentially formed on the hydrothermal treatments conducted with compositional variations between 7.5 mol to 50.0 mol% of Ti^{4+}. Indeed, some of the present authors reported the differences in the chemical reactivity of metal transition hydroxide gels in the alkaline hydrothermal media [20,21]. It deserves to emphasise that the crystallisation of cuboidal-shaped $SrZrO_3$ particles rapidly occurred using powders of $SrSO_4$ and $Zr(OH)_4^0$ dried gel in a 5 M KOH solution at 240 °C for 24 h, in comparison with an analogous reaction system employing a $Zr(OH)_4^0$ coprecipitated gel. The pasty hydroxide gel undergoes a dehydration process that markedly hinders the $SrSO_4$ dissolution; consequently, the bulk solute saturation proceeded slowly, triggering the nucleation of flower-shaped $SrZrO_3$ crystals. These crystals grew epitaxially along the [111] direction, resulting in large particles (mean size of 60 μm) for reaction intervals of 96 h [21].

By these results, we infer that the vigorous fluid agitation accelerated the $SrSO_4$ dissolution and the pasty $Zr(OH)_4^0$ gel dehydration, consequently triggering a rapid solute supersaturation within 4 h at a relatively low temperature of 200 °C, which rapidly provoked the crystallisation of $SrZrO_3$ cuboidal-shaped monodispersed crystals. The structural details determined by the TEM diffraction spot image indicated that the hydrothermally prepared $SrZrO_3$ crystals are single crystals in nature (Figure 8a). In contrast, the HR-TEM images depicted their high crystallinity, as confirmed by the 2D finger lattice atomic distribution. Interestingly, the observation conducted at the crystal edge in areas exhibiting $SrZrO_3$ fine particles grown on the surface indicated that the micron-sized $SrZrO_3$ single crystals grew epitaxially along the direction of the plane (112) that, corresponding to the lattice plane distance of 2.895 Å of the orthorhombic structure (card ICDD 70-0283). However, the dissolution-crystallisation mechanism provoked the SS1 and SS2 perovskite structured particles, irrespective of the $Ti(OH)_4 \bullet 4.5H_2O$ gel content. Likewise, the reactivity of the $Zr(OH)_4^0$ precursor gel seemingly proceeded faster when compared with the sample prepared solely with $Zr(OH)_4 \bullet 9.64H_2O$. The bulk alkalinity of the solvent fluid remains high when the Ti^{4+} concentration varies because the alkalinity reduction caused by the large water content released by the $Zr(OH)_4 \bullet 9.64H_2O$ dissolution is progressively hindered. Therefore, a specific reaction steady-state reaction is reached, triggering an accelerated solute supersaturation state that results in a fast crystallisation of orthorhombic (SS1) and cubic (SS2'), or solely the SS2 meso-crystals. Consequently, the primary crystal growth is hindered, as revealed by the HR-TEM micrographs taken for single-phase $SrZr_{0.5}Ti_{0.5}O_3$ and $SrTiO_3$ fine particles shown in Figure 8b and Figure 8c, respectively. These images also revealed features regarding the self-assembly process for primary anhedral nanosized crystals (20–45 nm), which proceeds along the {011} crystallographic planes of the cubic structure. We surmise that their surface facets favour the fine crystals assembly with (011) indexes, seemingly exhibiting low surface energy, allowing them to coalesce rapidly.

Preprints (www.preprints.org) | NOT PEER-REVIEWED | Posted: 6 July 2023 doi:10.20944/preprints202307.0412.v1

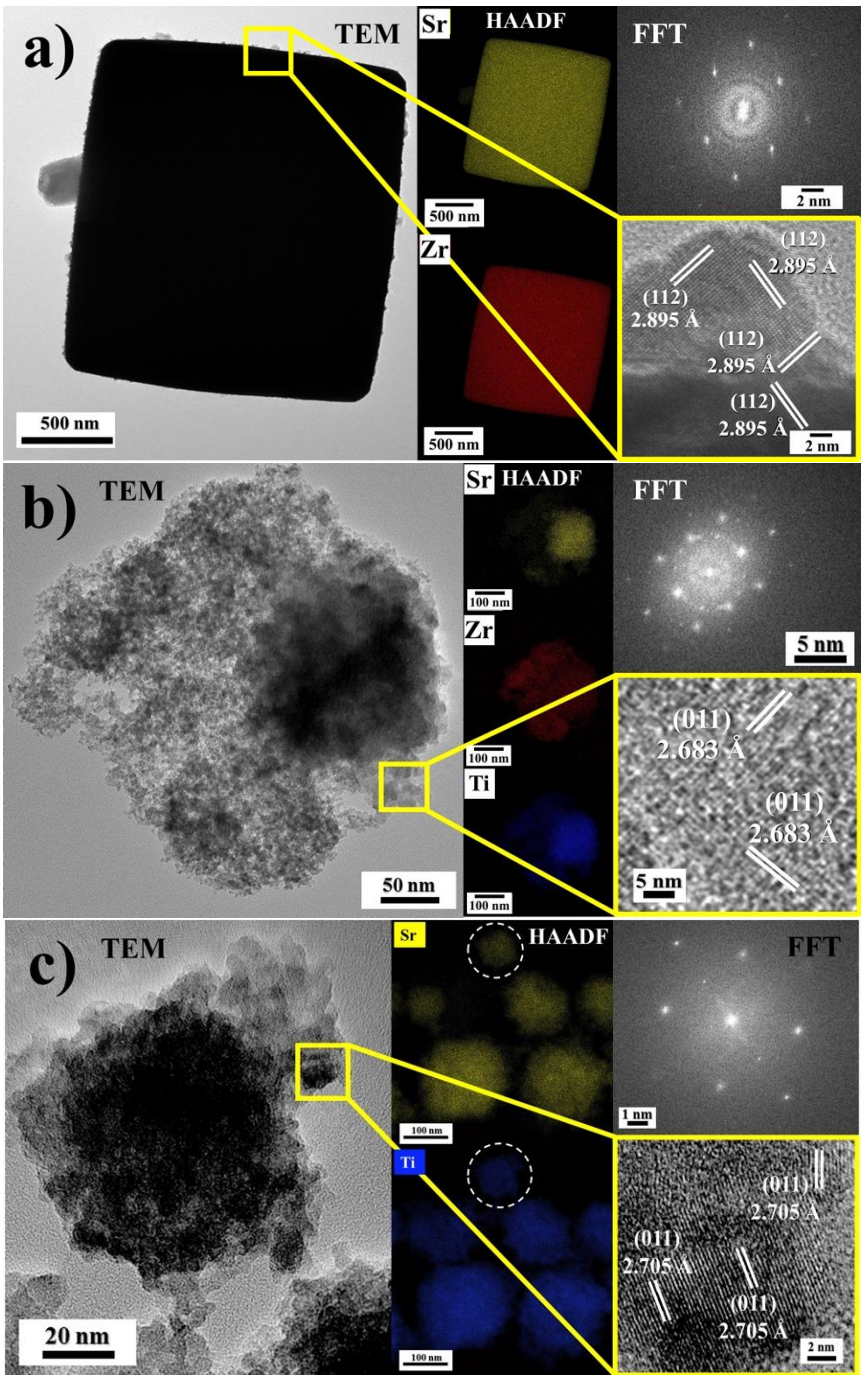

Figure 8. TEM micrographs of the SS $SrZr_{1-x}Ti_xO_3$ and $SrTi_{1-x}Zr_xO_3$ particles, obtained under hydrothermal conditions at 200 °C in a 5 M KOH for 4 h. The images correspond to single-phase samples of a) $SrZrO_3$, b) $SrZr_{0.5}Ti_{0.5}O_3$ and c) $SrTiO_3$.

Consequently, the 3D hierarchical assembly produces highly crystalline agglomerates with pseudocubic morphology. This inference is supported by 2D finger lattice atomic distribution images and FFT diffraction patterns, as shown in Figure 8b,c. These results revealed that the single-phase cubic structured $SrZr_{0.5}Ti_{0.5}O_3$ and $SrTiO_3$ primary crystals grew along (011) planes and subsequently coalesced to form the nanosized (140 – 175 nm) meso-crystals agglomerates, which exhibited single crystal areas as revealed by the FFT diffraction patterns. Interestingly, the 3D assembly process irrespectively proceeded by varying the Ti^{4+} content in the 7.5–100 mol% range. According to these results, we inferred that under hydrothermal conditions, the continuous vigorous stirring of the alkaline fluid triggered a homogeneous dispersion of the raw precursors ($SrSO_4$ powder and the mixture of the pasty gel species), yielding a controlled dissolution-crystallisation reaction carried out

in a single step to synthesise various perovskite solid solution in the binary system $SrZrO_3$–$SrTiO_3$. Indeed, the proposed soft chemistry process is faster than that even conducted under highly alkaline 5 M NaOH fluid to produce $SrZrO_3$ without stirring under hydrothermal conditions [21].

4. Conclusions

A systematic analysis of the formation of powders with varying contents of Zr^{4+} and Ti^{4+} ions was satisfactorily conducted in the binary system $SrZrO_3$–$SrTiO_3$. Various $SrZr_{1-x}Ti_xO_3$ and $SrTi_{1-x}Zr_xO_3$ solid solutions were rapidly crystallised under hydrothermal conditions at 200 °C for the shortest 4 h interval, with vigorous stirring (130 rpm) of the 5 M KOH solution. These conditions triggered the dissolution of low-grade powdered ore ($SrSO_4$) coupled with the mixture of hydrous Zr^{4+} and Ti^{4+} coprecipitated gels. The stable orthorhombic perovskite single phase ($SrZr_{1-x}Ti_xO_3$) incorporated a maximum content of Ti^{4+} of 7.5 mol%, while two different phases with orthorhombic (SS1) and cubic (SS2′) structures, corresponding to $SrZr_{1-x}Ti_xO_3$, were preferentially crystalised by varying the Ti^{4+} concentration between 7.5 to 47.5 mol% Ti^{4+}. The single phase of $SrTi_{1-x}Zr_xO_3$ with cubic structure was predominantly crystallised at higher contents, over 50.0 mol% Ti^{4+}. The synthesis of broadly selected particles with various compositions in the binary system $SrZrO_3$–$SrTiO_3$ was triggered by a massive dissolution–crystallisation mechanism of ionic species under alkaline hydrothermal conditions. However, this mechanism was affected by the partial decrease in the solvent alkalinity caused by the bulk water release during the dissolution of $Zr(OH)_4•9.64H_2O$ rather than the $SrSO_4$ powder or $Ti(OH)_4•4.5H_2O$ precursors. This process favoured a specific steady-state chemical reaction, triggering an optimum solute saturation that achieved simultaneous SS1 and SS2′ fine particle crystallisation.

The slow dissolution of the Zr-gel enhanced a remarkable growth of the $SrZrO_3$ particles exhibiting a cuboidal-shaped morphology and unimodal particle size distribution with a mean size of 3.8 μm. However, the particle crystallisation was rapidly triggered by adding the Ti-gel to the hydrothermal system, causing a remarkable particle size reduction for the intermediate orthorhombic (SS1) and cubic (SS2′) structured solid solutions crystallised. The meso-crystals particle sizes varied between 141.0–175.5 nm and exhibited a pseudo cubic morphology; these particles were formed by the spontaneous self-assembly of primary anhedral crystals with dimensions fluctuating between 10.0 nm to 20.0 nm. The 3D hierarchical assembly process preferentially occurred along the cubic crystallographic planes {011}, forming pseudocubic-shaped agglomerates. The meso-crystals corresponding to Ti^{4+}-rich perovskite solid solutions were produced via the same assembly process. Hence, these results suggest the potential application of the hydrothermal processing method employed in this work for processing other inorganic perovskite binary systems to tailor specific chemical compositions with enhanced functional properties.

Author Contributions: Conceptualization, J.C.R.A.; methodology and experiments J.C.R.A. and Z.M.V.; data analyses, J.R.Q.G. and Z.M.V.; writing—original draft preparation, J.C.R.A., J.L.C.; writing—review and editing, J.C.R.A., J.L.C. and R.P.G.; supervision, J.C.R.A and J.L.C.; funding acquisition, J.C.R.A and K.Y. All authors have read and agreed with the published version.

Funding: A part of this research was supported by federal research budget (C-3000-2019) of the Centre for Research and Advanced Studies of the NPI

Data Availability Statement: The data supporting this study's findings are available from the corresponding author upon reasonable request.

Acknowledgments: J.C.R.-A.; Z.M.-V.; J.L.-C and R.P.-G. are indebted to CONACYT-SNI. J.R.Q.-G is indebted to the PhD scholarship from CONACYT. Many thanks are also given to Dr Miguel Angel Aguilar-González and MSc Felipe de Jesus Marquez-Torres at the Center for Research and Advanced Studies for the NPI for their assistance on the FE-SEM and HR-TEM observations, respectively.

Conflicts of Interest: The authors declare no conflict of interest.

References

1. Bera, J.; Rout, S.K. $SrTiO_3$–$SrZrO_3$ solid solution: Phase formation kinetics and mechanism through solid-oxide reaction. *Mater. Res. Bull.* **2005**, 40, 1187–1193. https://doi.org/10.1016/j.materresbull.2005.03.029.
2. Vasala, S.; Karppinen. M. $A_2B'B''O_6$ perovskites: A review. *Prog. Solid State Chem.* **2015**, 43, 1–36. http://dx.doi.org/10.1016/j.progsolidstchem.2014.08.001.
3. Benedek, N.A.; Fennie, C.J. Why are there so few perovskite ferroelectrics? *J. Phys. Chem. C.* **2013**, 117, 13339−13349. https://doi.org/10.1021/jp402046t.
4. McKnight, R.E.A.; Kennedy, B.J.; Zhou, Q.; Carpenter, MA Elastic anomalies associated with transformation sequences in perovskites: II. The strontium zirconate–titanate $Sr(Zr,Ti)O_3$ solid solution series. *J. Phys.: Condens. Matter.* **2009**, 21, 015902. http://dx.doi:10.1088/0953-8984/21/1/015902.
5. Yang, Y.; Luo, S.; Dong, F.; Ding, Y.; Li, X. Synthesis of High-Phase Purity $SrTi_{1-x}Zr_xO_3$ Ceramics by Sol-Spray Pyrolysis Method. *Mater. Manuf. Processes.* **2015**, 30, 585–590. https://doi.org/10.1080/10426914.2014.984305.
6. Parida, S.; Rout, SK; Gupta, N.; Gupta, V.R. Solubility limits and microwave dielectric properties of $Ca(Zr_xTi_{1-x})O_3$ solid solution. *J. Alloys Compd.* **2013**, 546, 216–223. http://dx.doi.org/10.1016/j.jallcom.2012.08.076.
7. Chen, C.; Wei, Y.; Chen, D.; Jiao, X. $SrTi_{1-x}Zr_xO_3$ uniform particles: Low-temperature synthesis, characterisation and sintered properties. *J. Mater. Process. Technol.* **2008**, 205, 432–438. http://dx.doi:10.1016/j.jmatprotec.2007.11.202.
8. Wong, T.K.-Y.; Kennedy, B.J.; Howard, C.J.; Hunter, B.A.; Vogt, T. Crystal structures and phase transitions in the $SrTiO_3$-$SrZrO_3$ solid solution. *J. Solid State Chem.* **2001**, 156, 255–263. http://dx.doi:10.1006/jssc.2000.8896.
9. Shende, R.V.; Krueger, D.S.; Rossetti, G.A.; Lombardo, S.J. Strontium zirconate and strontium titanate ceramics for high-voltage applications: Synthesis, processing, and dielectric properties. *J. Am. Ceram. Soc.* **2001**, 84 (7), 1648–1650. http://dx.doi:10.1111/j.1151-2916.2001.tb00893.x.
10. Wu, Z.; Cao, M.; Yu, H.; Yao, Z.; Luo, D.; Liu, H. The microstructures and dielectric properties of $xSrZrO_3$–$(1-x)SrTiO_3$ ceramics. *J. Electroceram.* **2008**, 21, 210–213. http://dx.doi:10.1007/s10832-007-9103-9.
11. Zhang, Z.; Koppensteiner, J.; Schranz, W.; Carpenter, MA Anelastic loss behaviour of mobile microstructures in $SrZr_{1-x}Ti_xO_3$ perovskites. *J. Phys.: Condens. Matter.* **2010**, 22, 295401, 1–8. http://dx.doi:10.1088/0953-8984/22/29/295401.
12. Christen, H.M.; Knauss, L.A.; Harshavardhan, K.S. Field-dependent dielectric permittivity of paraelectric superlattice structures. *Mater. Sci. Eng. B.* **1998**, 56, 200–203. https://doi.org/10.1016/S0921-5107(98)00237-2.
13. Yugami, H.; Iguchi, F.; Naito, H. Structural properties of $SrCeO_3$ /$SrZrO_3$ proton conducting superlattices. *Solid State Ionics*. **2000**, 136–137, 203–207. https://doi.org/10.1016/S0167-2738(00)00307-6.
14. Longo V.M.; Cavalcante, L.S.; Costa, M.G.S.; Moreira, M.L.; De Figueiredo, A.T.; Andrés, J.; Varela, J.A.; Longo, E. First principles calculations on the origin of violet-blue and green light photoluminescence emission in $SrZrO_3$ and $SrTiO_3$ perovskites. *Theor. Chem. Acc.* **2009**, 124, 385–394. http://dx.doi:10.1007/s00214-009-0628-7.
15. Celik, G.; Cabuk, S. First-principles study of electronic structure and optical properties of $Sr(Ti,Zr)O_3$. *Cent. Eur. J. Phys*. **2013**, 11(3), 387–393. http://dx.doi:10.2478/s11534-013-0176-6.
16. Khunrattanaphon, P.; Chavadej, S.; Sreethawong, T. Synthesis and application of novel mesoporous-assembled $SrTi_xZr_{1-x}O_3$-based nanocrystal photocatalysts for azo dye degradation. Chem. Eng. J. 2011, 170, 292–307. http://dx.doi:10.1016/j.cej.2011.03.055.
17. Kalyani, V.; Vasile, B.S.; Ianculescu, A.; Buscaglia, M. T.; Buscaglia, V.; Nanni, P. Hydrothermal synthesis of $SrTiO_3$ mesocrystals: single crystal to mesocrystal transformation induced by topochemical reactions. Cryst. Growth Des. 2012, 12, 4450–4456. http://dx.doi.org/10.1021/cg300614f.
18. Huang, S.T.; Lee, W.W.; Chang, J.L.; Huang, W.S.; Chou, S.Y.; Chen, C.C. Hydrothermal synthesis of $SrTiO_3$ nanocubes: Characterisation, photocatalytic activities, and degradation pathway. J. Taiwan Inst. Chem. Eng. 2014, 45, 1927-1936. http://dx.doi.org/10.1016/j.jtice.2014.02.003.
19. Kalyani, V.; Vasile, B.S.; Ianculescu, A.; Testino, A.; Carino, A.; Buscaglia, M. T.; Buscaglia, V.; Nanni, P. Hydrothermal synthesis of $SrTiO_3$: role of interfaces. Cryst. Growth Des. 2015, 15, 5712–5725. http://dx.doi.org/10.1021/acs.cgd.5b00770.

20. Rangel-Hernandez, Y.M.; Rendón-Angeles J.C.; Matamoros-Veloza, Z.; Pech-Canul, M.I.; Diaz-de la Torre, S.; Yanagisawa, K. One-step synthesis of fine $SrTiO_3$ particles using $SrSO_4$ ore under alkaline hydrothermal conditions. Chem. Eng. J. 2009, 155, 483–492. http://dx.doi:10.1016/j.cej.2009.07.024.
21. Quiñones-Gurrola, J.R.; Rendón-Angeles, J.C.; Matamoros-Veloza, Z.; Rodríguez-Galicia, J.L., Yanagisawa, K. Rapid one-step preparation of $SrZrO_3$ using Zr^{4+} gel and $SrSO_4$ ore under alkaline hydrothermal conditions, Bol. Soc. Esp. Cerám. Vidr. 2023, in press. https://doi.org/10.1016/j.bsecv.2022.12.002.
22. Mourão, H.A.J.L.; Lopes, O.F.; Ribeiro, C.; Mastelaro, V.R. Rapid hydrothermal synthesis and pH-dependent photocatalysis of strontium titanate microspheres, Mater. Sci. Semicond. Process. 30 (2015) 651–657. https://dx.doi.org/10.1016/j.mssp.2014.09.022.
23. Rendón-Angeles, J.C.; Matamoros-Veloza, Z.; Gonzalez, L.A.; López-Cuevas, J.; Ueda, T.; Yanagisawa, K.; Hernández-Calderón I.; Garcia-Rocha, M. Rapid hydrothermal synthesis of $SrMo_{1-x}W_xO_4$ powders: Structure and luminescence characterization. Advanced Powder Technology 2017, 28, 629-640. http://dx.doi.org/10.1016/j.apt.2016.11.015.